



Correlating the three-dimensional atomic defects and electronic properties of two-dimensional transition metal dichalcogenides

Xuezheng Tian^{1,8}, Dennis S. Kim^{1,8}, Shize Yang^{1,2,6,8}, Christopher J. Ciccarino^{3,4}, Yongji Gong⁵, Yongsoo Yang^{1,7}, Yao Yang¹, Blake Duschatko³, Yakun Yuan¹, Pulickel M. Ajayan⁵, Juan Carlos Idrobo^{1,2}, Prineha Narang^{1,3} and Jianwei Miao¹✉

The electronic, optical and chemical properties of two-dimensional transition metal dichalcogenides strongly depend on their three-dimensional atomic structure and crystal defects. Using Re-doped MoS₂ as a model system, here we present scanning atomic electron tomography as a method to determine three-dimensional atomic positions as well as positions of crystal defects such as dopants, vacancies and ripples with a precision down to 4 pm. We measure the three-dimensional bond distortion and local strain tensor induced by single dopants. By directly providing these experimental three-dimensional atomic coordinates to density functional theory, we obtain more accurate electronic band structures than derived from conventional density functional theory calculations that relies on relaxed three-dimensional atomic coordinates. We anticipate that scanning atomic electron tomography not only will be generally applicable to determine the three-dimensional atomic coordinates of two-dimensional materials, but also will enable ab initio calculations to better predict the physical, chemical and electronic properties of these materials.

Due to the reduced dimensionality, the properties and functionality of two-dimensional (2D) materials and van der Waals heterostructures are strongly influenced by atomic defects such as dopants, vacancies, dislocations, grain boundaries, strains, ripples and interfaces^{1–8}. Although aberration-corrected electron microscopy and scanning probe microscopy can image these materials at atomic resolution, they only provide 2D projection images or surface atomic structures^{1,6–10}. Atomic electron tomography (AET) allows the determination of three-dimensional (3D) atomic structure of crystal defects and chemical disorder systems^{11–17}, and has recently been advanced to observe crystal nucleation at four-dimensional atomic resolution¹⁸. However, AET has thus far been limited to metallic nanoparticles and needle-shaped samples. Application of AET to 2D materials is essential for accurate 3D atomic structure characterization, but requires three obstacles to be overcome. First, these materials are electron-beam sensitive and the experiments must be performed with low electron doses^{1,2}. Second, due to the geometric constraint of 2D materials and their suspended nature, the tilt range of data acquisition is limited in aberration-corrected electron microscopy¹⁹. Third, the 3D precision of experimental atomic coordinates must be on the picometre scale so that they can be used as direct input to density functional theory (DFT) calculations to reveal physical, chemical and electronic properties^{20–22}. Here, we develop scanning atomic electron tomography (sAET) to overcome these limitations and determine the 3D coordinates of individual atoms in Re-doped MoS₂ monolayers with picometre precision. We identify 3D crystal defects such as dopants,

vacancies and atomic-scale ripples, and measure the 3D bond distortion and local strain tensor induced by single Re dopants. We show that the experimental 3D atomic coordinates can be used as direct input to DFT calculations to derive more truthful electronic band structures than obtained from conventional DFT with relaxed atomic coordinates.

Scanning atomic electron tomography

Doping in semiconductors has been an important tool for tailoring their chemical, optical and electronic properties. However, due to the reduced dimensionality, doping in 2D materials is beyond a simple substitutional electron donor or acceptor. In Mo-based 2D transition metal dichalcogenides (TMDs), for example, Re dopants have been identified as a good candidate for n-type doping^{23,24}. A high concentration of Re dopants in MoS₂ monolayers led to the phase transition from a trigonal prismatic (1H) structure to a distorted octahedral (1T') structure, which increases catalytic activity²⁵. However, a fundamental understanding of how the early-stage phase transition takes place at the atomic scale remains absent. To shed light on how single dopants in 2D TMDs perturb their 3D local structure and induce local strain tensor, we conducted sAET experiments using an aberration-corrected scanning transmission electron microscope (STEM), operated at 60 kV with an annular dark-field mode (ADF) detector. Two data sets were collected from the Re-doped MoS₂ monolayer, each consisting of 13 projections with small double-tilt ranges at a low dose (Supplementary Figs. 1 and 2 and Supplementary Table 1).

¹Department of Physics & Astronomy and California NanoSystems Institute, University of California, Los Angeles, CA, USA. ²Center for Nanophase Materials Sciences, Oak Ridge National Laboratory, Oak Ridge, TN, USA. ³John A. Paulson School of Engineering and Applied Sciences, Harvard University, Cambridge, MA, USA. ⁴Department of Chemistry and Chemical Biology, Harvard University, Cambridge, MA, USA. ⁵Department of Materials Science and NanoEngineering, Rice University, Houston, TX, USA. ⁶Present address: Eyring Materials Center, Arizona State University, Tempe, AZ, USA. ⁷Present address: Department of Physics, Korea Advanced Institute of Science and Technology, Daejeon, Korea. ⁸These authors contributed equally: Xuezheng Tian, Dennis S. Kim, Shize Yang. ✉e-mail: miao@physics.ucla.edu

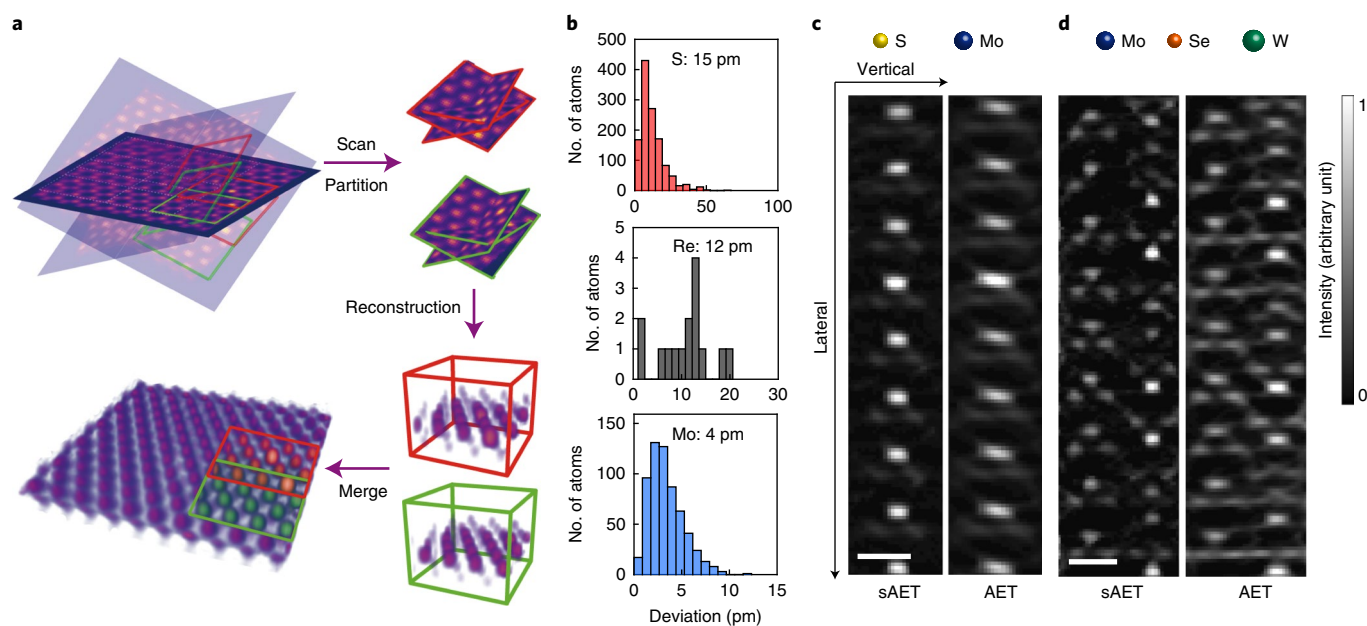


Fig. 1 | Scanning atomic electron tomography. **a**, A number of projections were acquired from a 2D material or heterostructure with different tilt angles. A 3D window of $60 \times 60 \times 60$ voxels in this case was chosen to locate the corresponding region in each of the 13 projections (red frames). The window was scanned along the x and y axes with a step size of 30 voxels (green frames). At each step, the corresponding regions in the projections for each window were identified. After all the projections were partitioned into a series of image stacks, the 3D windows were reconstructed from the image stacks and stitched together to form a full reconstruction. **b**, Histograms of the deviation between the experimental and multislice simulation 3D atomic models for 1,226 S, 15 Re and 611 Mo atoms with the RMSD shown in each histogram. **c**, sAET and AET reconstructions of an experimental Re-doped MoS_2 data set, showing that sAET improves the 3D atomic shapes over AET. Scale bar, 5 Å. **d**, sAET and AET reconstructions of an MoSe_2 - WSe_2 heterostructure with moiré patterns from 15 multislice projections. The MoSe_2 - WSe_2 heterostructure has a 5° rotational mismatch between the top and bottom layers. The side-view image shown here is aligned with the MoSe_2 layer and slices through the centre of the Mo and Se atoms with a thickness of 1 Å. A full top view of the reconstruction is shown in Extended Data Fig. 5. The 3D precision of determining the Mo, W and Se atomic positions by sAET was estimated to be 8 pm, 5 pm and 13 pm, respectively, while the atomic shapes in the AET reconstruction are elongated. Scale bar, 5 Å.

After processing the two data sets (Methods and Supplementary Figs. 3 and 4), we performed sAET reconstruction of aligned projections (Fig. 1a). sAET takes advantage of the relationship $d \propto \frac{D}{N}$, where d is the 3D resolution, D is the size of an object to be reconstructed and N is the number of projections²⁶. For a small N limited by the electron dose, we can improve d by reducing D . Although symmetry in the object can also be used to improve resolution²⁷, we chose not to apply this constraint because we wanted to determine 3D crystal defects in 2D TMDs at the single-atom level. To implement sAET, we partitioned all the projections into small image stacks with 3D windows (Fig. 1a); each 3D window was reconstructed by the generalized Fourier iterative reconstruction (GENFIRE) algorithm²⁸. All the 3D windows were then stitched together to form a full reconstruction, where the overlap volume between neighbouring windows containing artefacts due to boundary effects was discarded (Methods). Extended Data Figs. 1 and 2 and Supplementary Video 1 show the reconstructions of data sets 1 and 2, where all the Re dopants are direct replacements for Mo atoms. The side-view images in Extended Data Fig. 1a (inset) illustrate the intensities of Mo, S and Re atoms, with S vacancies indicated by arrows. From each reconstruction, the 3D atomic coordinates and chemical species were traced, refined and corroborated (Methods, Extended Data Figs. 1b and 2b and Supplementary Video 2).

To estimate the 3D precision of the atomic positions, we implemented two independent methods for cross-validation. First, we identified the x and y coordinates of the Re and Mo atoms in each projection of the data sets using a Gaussian fit (Extended Data Fig. 3a), whereas the positions of individual S atoms could not be accurately localized from an individual 2D projection due to their weak contrast in ADF images. From these 2D coordinates of Re and

Mo atoms, we used least-square fitting to calibrate the tilt angles (Supplementary Table 2) and determine their 3D atomic coordinates (Extended Data Fig. 3b). The Re and Mo atomic coordinates are consistent with those obtained by sAET with root mean square deviations (RMSDs) of 13 pm and 2 pm, respectively (Extended Data Fig. 3c, d). Second, we performed multislice simulations to calculate 13 projections from the experimental 3D atomic model (Methods and Extended Data Fig. 4). By applying the same reconstruction, atom tracing and refinement procedures, we obtained a new 3D atomic model from the 13 multislice projections with all atoms and defects correctly identified. The RMSDs between the experimental and new atomic models are 15 pm, 12 pm and 4 pm for S, Re and Mo atoms, respectively (Fig. 1b). The 3D precision of the Re and Mo atoms is consistent with those obtained by the least-square fitting method.

To show the advantage of sAET over AET for the 3D reconstruction of 2D TMDs, we reconstructed the experimental Re-doped MoS_2 data sets using AET (Fig. 1c). Due to the small tilt range and the limited number of projections, all atoms in the AET reconstruction are elongated along the z axis (the beam direction). This atom elongation problem is alleviated by sAET (Fig. 1c), allowing more precise determination of the 3D coordinates of individual atoms. To demonstrate the applicability of sAET to van der Waals heterostructures, we performed numerical simulations on the 3D reconstruction of a MoSe_2 - WSe_2 heterojunction with a 5° rotational mismatch between the top and bottom layers. This type of heterostructure has recently received considerable attention due to its moiré exciton properties^{29,30}. Using multislice simulations, we calculated a tilt series of 15 projections from the heterostructure consisting of atomic defects (Methods). From the same data, we reconstructed

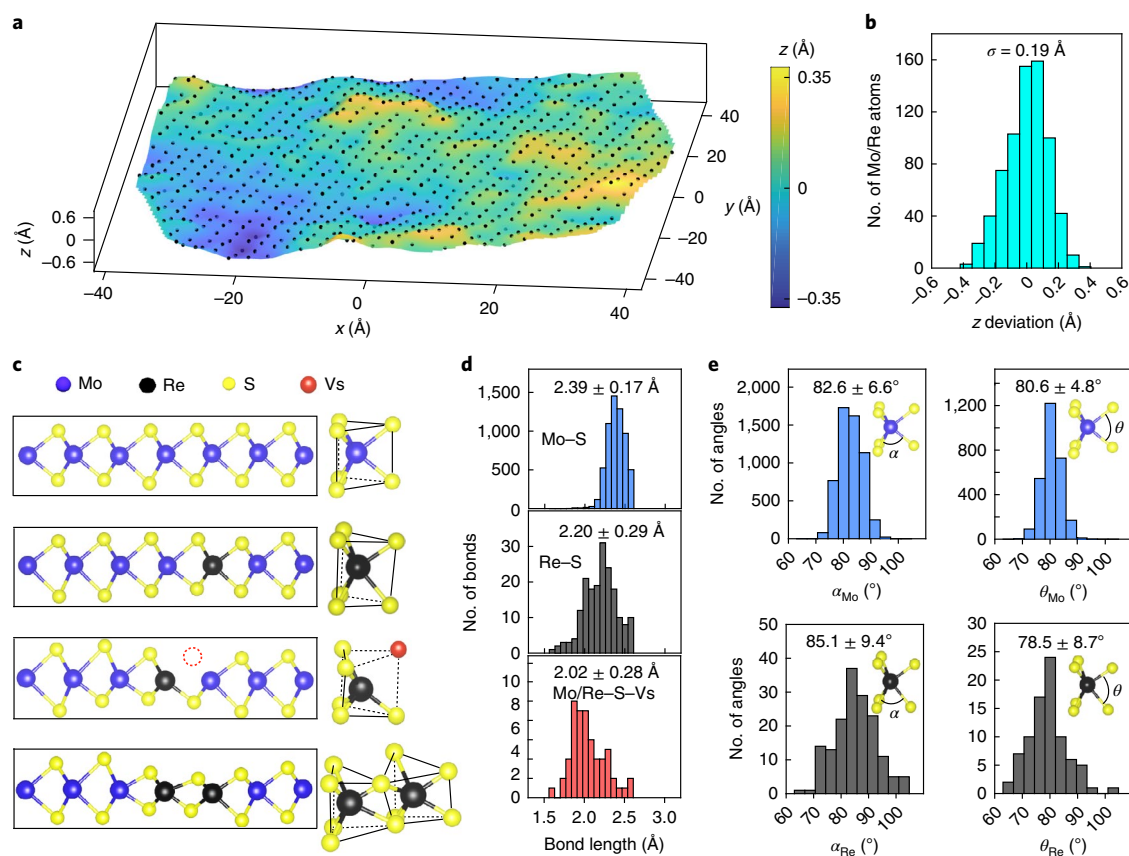


Fig. 2 | 3D atomic coordinates in Re-doped MoS₂ and 3D bond distortion induced by single dopants. a, 3D atomic-scale ripples in data set 1, where the dots represent the Mo/Re atoms. The total numbers of Re, Mo and S atoms and S vacancies in the data set are 21, 686, 1,381 and 15, respectively. **b**, Histogram of the distribution of the *z* coordinates of the Mo/Re atoms in data set 1 with a standard deviation (σ) of 19 pm. **c**, Magnified views of four configurations cropped from the 3D coordinates showing the 3D bond distortion: MoS₂ (top), MoS₂ with a single Re dopant (second panel), MoS₂ with a Re–vacancy pair (third panel) and MoS₂ with two Re dopants (bottom), where the red circle and sphere represent a S vacancy. In each case, the six coordinating S atoms (yellow spheres) are shown in the right-hand panels. **d**, Statistical distributions of the Mo–S and Re–S bond lengths as well as the shortened bond length if there is a S vacancy in the opposite S layer. For reference, the Mo–S bond length of a perfect 1H structure is 2.36 Å. **e**, Statistical distributions of the bonding angles around Mo (top panels) and Re atoms (bottom panels): α is the inner angle of two neighbouring S atoms in the same atomic layer and θ is the inner angle of a pair of S atoms from opposite atomic layers. For reference, the corresponding angles of a perfect 1H structure are $\alpha = 83.8^\circ$ and $\theta = 79.1^\circ$.

and traced the 3D atomic positions using sAET and AET. Extended Data Fig. 5 shows the sAET reconstruction and the traced atomic positions in six atom layers, which are in good agreement with the original 3D atomic model. The RMSDs between the sAET reconstruction and the original atomic model are 8 pm, 5 pm and 13 pm for Mo, W and Se atoms, respectively. However, the atomic shapes in the AET reconstruction are elongated along the *z* axis (Fig. 1d). These results show the unique advantage of sAET over AET to determine the 3D atomic positions in 2D TMDs, because these materials have much larger *x* and *y* dimensions than *z* dimension. The number of projections required by sAET is proportional to the thickness of the *z* dimension. Only when the *z* dimension reaches the same size as the *x* and *y* dimensions will sAET have no advantage over AET.

Measuring the 3D bond distortion and local strain tensor

From the experimental 3D atomic coordinates, we observed atomic-scale ripples and estimated the standard deviation of the Mo and Re atoms along the *z* axis to be 19 pm and 16 pm for data sets 1 and 2, respectively (Fig. 2a,b and Extended Data Fig. 2c,d). The magnitude and wavelength of the ripples in Re-doped MoS₂ are within the range of previously reported values^{31–37}. Compared with other techniques to characterize ripples in 2D materials^{31–37},

sAET is a real-space method that can reveal 3D atomic-scale ripples with picometre precision. This high precision allowed us to measure the 3D bond distortion induced by single dopants. We found that the Re–Re pair and the Re–S vacancy pair induce larger distortion than single Re dopants (Fig. 2c). We determined the Mo–S and Re–S bond lengths to be 2.39 ± 0.17 Å and 2.20 ± 0.29 Å, respectively (Fig. 2d). Statistically, the Re–S bond is 19 pm shorter than the Mo–S bond. With S vacancies, the opposite Re/Mo–S bond length was reduced to 2.02 ± 0.28 Å (Fig. 2d). Although there are only 37 Re dopants in the two data sets, we found that 10 out of a total of 19 S vacancies are situated next to the Re dopants, which is due to the lower vacancy formation energy of neighbouring Re dopants^{23–25}. Furthermore, we also determined the deviation of the bond angles from the 1H structure. The angles between the Re–S bonds in the same and opposite atomic layer are $85.1 \pm 9.4^\circ$ and $78.5 \pm 8.7^\circ$, respectively, whereas the corresponding angles of the Mo–S bonds are $82.6 \pm 6.6^\circ$ and $80.6 \pm 4.8^\circ$, respectively (Fig. 2e).

Next, we measured the 3D atomic displacements and the full strain tensor of the 2D TMD (Methods). Figure 3a–c shows the displacements of the Mo and Re atoms in data set 1 along the *x*, *y* and *z* axes, respectively. Figure 3d–i and Extended Data Fig. 6 show the six components of the strain tensor in three atomic layers, where we observed both the non-local and local strain tensor. The non-local

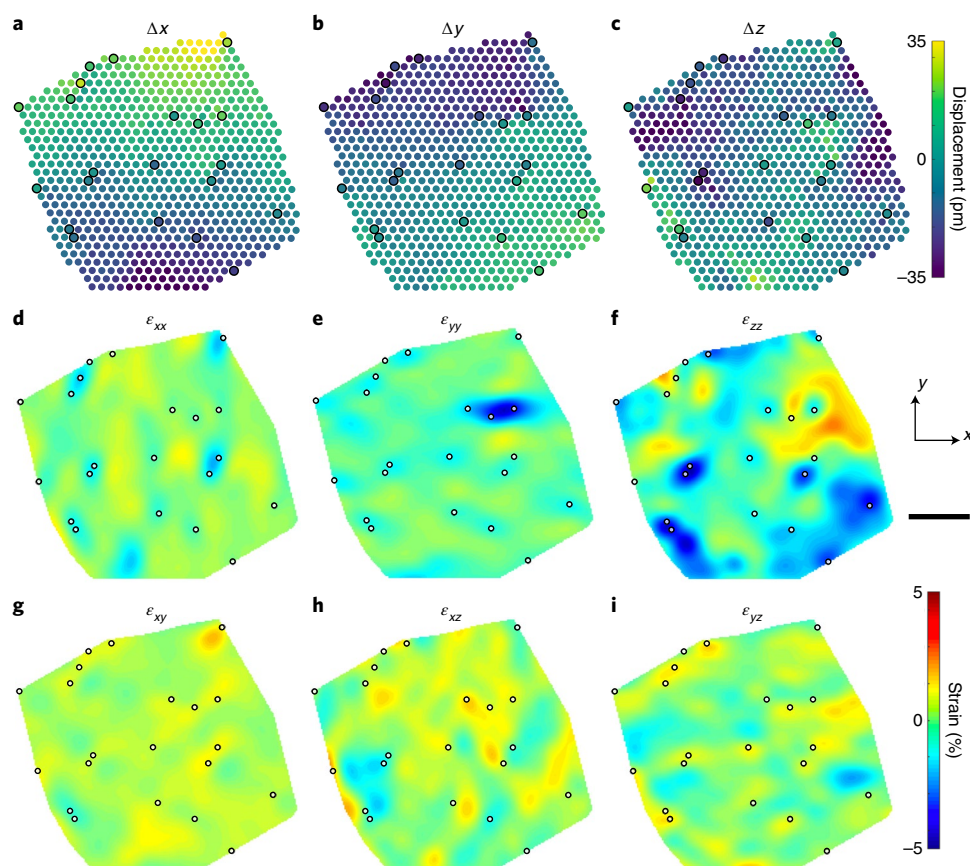


Fig. 3 | Measurements of 3D atomic displacements and the full strain tensor in Re-doped MoS₂. **a–c**, 3D atomic displacements of Mo (dots) and Re (circled dots) atoms along the *x*, *y* and *z* axes, respectively. **d–i**, Six components of the strain tensor in the Mo/Re layer, where the Re dopants (circles) induce local strains in the ϵ_{xx} , ϵ_{yy} and ϵ_{zz} maps. The *x*, *y* and *z* axes are along the [1,0,0], [1,2,0] and [0,0,1] directions, respectively. The strain tensor of the two S layers is shown in Extended Data Fig. 6. Scale bar, 2 nm.

strain was induced by the flexibility and thinness of the 2D TMD suspended on a TEM grid. To decouple the non-local and local strain tensor, we chose spheres with a radius of 3.16 Å centred at Re and Mo atoms in the two data sets. We measured the local strain tensor within the spheres and observed that the changes of the ϵ_{xx} , ϵ_{yy} and ϵ_{zz} components between the Re and Mo atom spheres are 0.82%, 0.82% and 1.15%, respectively, while the changes of the ϵ_{xy} , ϵ_{xz} and ϵ_{yz} components are small (Fig. 4).

These results enable us to understand the dopant-induced phase transition in MoS₂ at the single-atom level. Previous studies have reported the phase transition of MoS₂ from the 1H structure to the 1T' structure with a high concentration of Re dopants^{23–25}. However, how the early-stage phase transition initiates at the single dopant remains unknown. According to the crystal field theory³⁸, the electronic structure and preferred phase of TMDs strongly depend on the coordination environment of the transition metal and the *d* electrons^{38,39}. As a group 6 TMD, MoS₂ has two non-bonding *d* electrons (*d*²), which prefer to fill the *d*_{z²} orbital of the 1H phase in ambient conditions. However, Re has three non-bonding *d* electrons (*d*³) and tends to form an octahedral phase in a TMD³⁸. The extra *d* electrons from Re dopants in MoS₂ fill higher energy levels of the 1H phase (*d*_{xy} and *d*_{x²–y²} orbitals), which destabilizes and distorts the 1H phase towards an octahedral phase^{25,39–41}. Thus, our experimental results (Fig. 3 and Extended Data Fig. 6) provide direct structural information to understand the dopant-induced phase transition at the single-atom level. The local distortion created by Re dopants is expected to have important consequences for the electronic properties of the 2D TMD.

Correlating crystal defects with electronic band structures

To correlate 3D crystal defects with the electronic band structure of the Re-doped MoS₂ monolayer, we selected four supercells in different regions of data set 1 (Fig. 5e). The experimental 3D atomic coordinates of each supercell were used as direct input to DFT to determine the effective band structure of each supercell and reveal the underlying electronic symmetries via band-unfolding techniques (Supplementary methods). For comparison, the same experimental atomic coordinates were relaxed to obtain the equilibrium band structures using DFT (Fig. 5a–d, middle). The band structures obtained directly from the experimental coordinates show highly distorted indirect band gaps or metal-like behaviour with a large number of shadow bands. In contrast, the band structures of the relaxed experimental coordinates exhibit direct band gaps with considerably reduced shadow bands⁴². This behaviour is consistent throughout the Brillouin zone, as seen in each supercell density of states (DOS) shown to the right of each band-structure calculation (Fig. 5a–d).

Strain is known to strongly influence the band structure of 2D TMDs^{5,7}. To study the effects of the local strain on the band structure, we calculated the principal strains by solving for the eigenvalues and eigenvectors of the strain tensor within each supercell. The principal strains of Fig. 5a–d indicate that the increase of the local strain breaks the local symmetry and generates more shadow bands (Methods and Extended Data Fig. 7). In addition to shadow bands, we also observed defect states in the band structure of the supercell containing one Re dopant (Fig. 5b left and middle), whereas more defect states appear in the band gap of the supercell with two Re

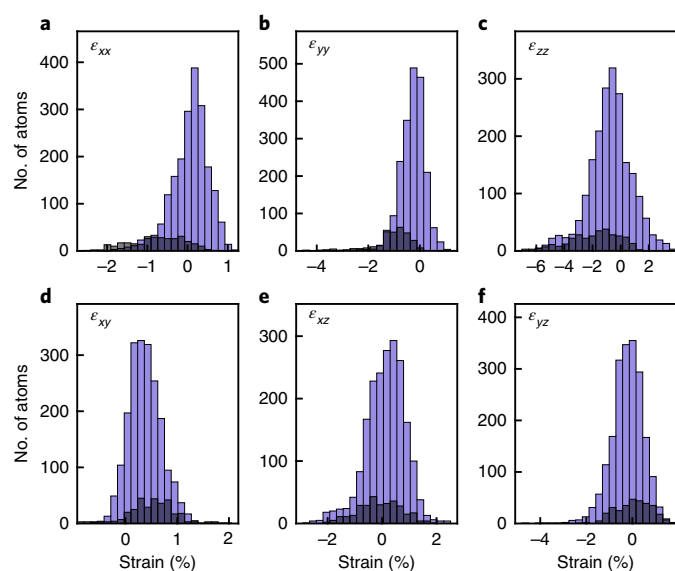


Fig. 4 | Measurements of the local strain tensor induced by single Re dopants. a–f, Histograms of the distribution of the six strain components: ϵ_{xx} , ϵ_{yy} , ϵ_{zz} , ϵ_{xy} , ϵ_{xz} and ϵ_{yz} around Mo (purple) and Re (black) atoms. To decouple the non-local and local strain tensor, spheres with a radius of 3.16 Å were chosen centred at the Mo and Re atoms. The distributions of the six strain components within the Mo atom spheres were determined to be $\epsilon_{xx} = 0.06 \pm 0.45$, $\epsilon_{yy} = -0.28 \pm 0.48$, $\epsilon_{zz} = -0.73 \pm 1.54$, $\epsilon_{xy} = 0.38 \pm 0.32$, $\epsilon_{xz} = 0.12 \pm 0.72$ and $\epsilon_{yz} = -0.21 \pm 0.69$, whereas the distributions of the six strain components within the Re atom spheres were estimated to be $\epsilon_{xx} = -0.76 \pm 0.67$, $\epsilon_{yy} = -1.1 \pm 0.77$, $\epsilon_{zz} = -1.88 \pm 1.75$, $\epsilon_{xy} = 0.41 \pm 0.49$, $\epsilon_{xz} = -0.1 \pm 0.78$ and $\epsilon_{yz} = 0.02 \pm 0.77$. The changes of the ϵ_{xx} , ϵ_{yy} , ϵ_{zz} , ϵ_{xy} , ϵ_{xz} and ϵ_{yz} components between the Re and Mo atom spheres are 0.82%, 0.82%, 1.15%, 0.03%, 0.22% and 0.23%, respectively.

dopants (Fig. 5c left and middle). The striking differences between the band structures of the experimental and relaxed atomic coordinates suggest that the experimental structure is in a metastable state due to the complex strain distribution induced by 3D crystal defects and the interactions with the rest of the lattice, while the relaxed structure is in the global equilibrium state. The metastable structure is feasible, as Re dopants in MoS₂ produce defect wave functions that delocalize with slowly decaying tails⁴³. This delocalization of defect states with increasing concentration in various clusters of dopants results in a metastable structure, which clearly exhibits different electronic band structures (Fig. 5a–d). To quantitatively analyse the band structure, we averaged the DOS of the experimental structures in the four supercells (Fig. 5f, black curve), where the defect states and shadow bands from different energies and regions fill in the band gap. For comparison, Fig. 5f (red curve) shows the average DOS of the relaxed structures in the four supercells, where defect states due to the Re dopants and S vacancies still appear within the band gap, but not to the extent of the average DOS of the experimental structures (black curve). As a reference, the DOS of the relaxed MoS₂ structure is shown in Fig. 5f (blue curve). Although the DOS was obtained from four supercells, on the basis of the strain maps we expect a similar result if the whole sample is used for DOS calculations.

To experimentally study the effect of the band structure, we measured photoluminescence (PL) and Raman spectra of Re-doped MoS₂ and pristine MoS₂ monolayers synthesized under the same conditions (Supplementary methods, Fig. 5g and Supplementary Figs. 5 and 6). After examining several Re-doped MoS₂ monolayer samples, we found that most of the PL spectra were quenched, with no visible peak above the background. Figure 5g (black curve)

shows the only measured PL spectrum with a very weak exciton peak. The scale of the Re-doped MoS₂ spectrum relative to the background and pristine MoS₂ is shown in Supplementary Fig. 5. Compared with the pristine MoS₂ data (Fig. 5g, blue curve), the Re-doped MoS₂ spectrum exhibits much lower peak intensity, with the peak position only slightly shifted towards lower energies. This observation agrees with our effective band-structure calculations (Fig. 5f). Each region in Fig. 5 creates defect states within the gap at different energies, essentially creating a metal-like DOS. However, the density within the gap is relatively low and a semiconductor band gap can be realized. From the DOS calculations, we expect only a small feature visible in the PL spectrum, as the system is a highly distorted indirect-band-gap semiconductor, or metal-like behaviour (Fig. 5f). This is consistent with our experimental measurements, as certain regions show a small peak (Fig. 5g) and most are quenched spectra. Supplementary Fig. 6 shows the Raman spectra of the Re-doped MoS₂ and pristine MoS₂ monolayers. For both the in-plane and out-of-plane phonon modes, the peak intensity measured from Re-doped MoS₂ is about one-third of that from pristine MoS₂ (Supplementary Fig. 6). The peak intensity reduction in Re-doped MoS₂ indicates that the long-range order of the 1H structure of MoS₂ has been highly distorted by Re dopants, as confirmed by our direct experimental measurements (Figs. 2–4).

Our results demonstrate that doping in 2D TMDs depends not only on the concentration, but also on the local bonding characteristics and the equilibrium phase of the dopants. For example, WS₂ with a few per cent Nb dopants is a p-type direct-band-gap semiconductor with a strong PL peak⁴⁴, whereas both NbS₂ and WS₂ have the 1H structure. However, MoS₂ with a similar Re dopant concentration exhibits a quenched PL spectrum (Fig. 5g), whereas MoS₂ has the 1H structure and ReS₂ has the 1T' structure. The difference in local bonding and equilibrium phase of the dopants appears to account for these stark differences in doping effects at similar concentrations. Furthermore, at a sufficiently lower dopant concentration (0.3%), Re-doped MoS₂ is a simple n-type direct-band-gap semiconductor, whereas the PL peak shifts towards higher energies and there is no loss in peak intensity relative to pristine MoS₂ (ref. 44). Although the overall structural phase transition from the 1H to 1T' structure for Re-doped MoS₂ takes place around 40–50% doping^{25,45}, our results indicate that the effects on electronic properties induced by dopants occur at far lower concentrations.

Outlook

We developed sAET to determine the 3D atomic coordinates of 2D TMDs with picometre precision. We identified 3D crystal defects such as dopants, vacancies and ripples, and measured the 3D bond distortion and local strain tensor induced by single dopants. We used the experimental 3D atomic coordinates as direct input to DFT to reveal the electronic band structures of the 2D TMD, which were corroborated by PL measurements. Compared with other techniques that can image the 3D structure of graphene from only one or two images^{34,46,47}, both our experimental and numerical simulation results demonstrate that sAET is a more general method to determine the 3D atomic coordinates of 2D materials and van der Waals heterostructures with high precision. Furthermore, the combination of sAET and ptychography is expected to improve the 3D precision of localizing individual atoms and reduce the electron dose^{48,49}.

Our study reveals that single Re dopants in MoS₂ can create 3D local bond distortion and induce a local strain tensor. Due to the reduced dimensionality, the local strain along the *z* axis was measured to be larger than that along the *x* and *y* axes (Fig. 4). To engineer 2D TMDs with desired physical, chemical and electronic properties at the atomic scale, it is important to characterize and control the atomic structure in three dimensions. Furthermore, we show the necessity and importance of directly providing experimental

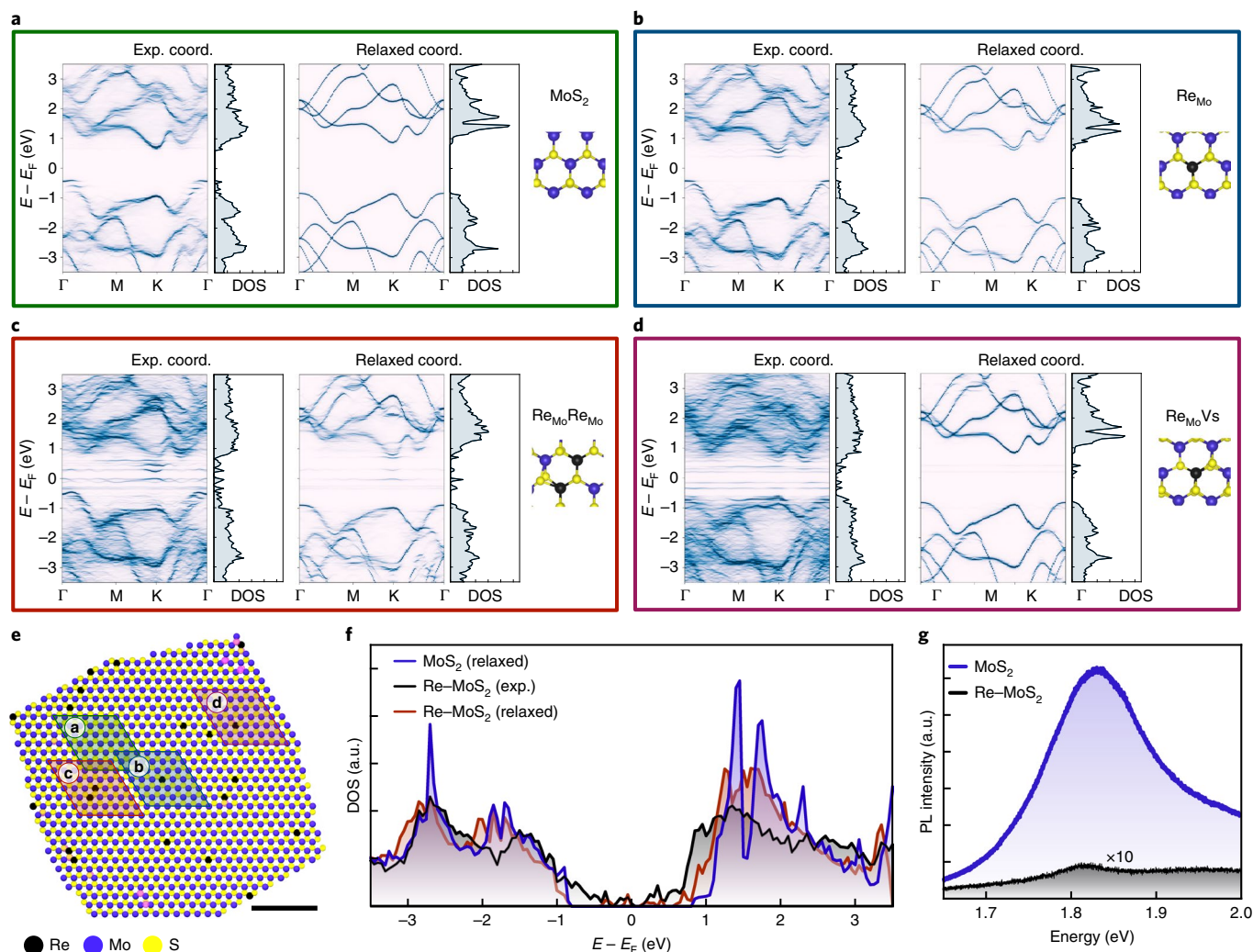


Fig. 5 | Electronic band structures calculated from experimental coordinates and PL measurements. **a–d**, Electronic band structures calculated from experimental 3D atomic coordinates, each consisting of $6 \times 6 \times 1$ unit cells, including a dopant-free MoS₂ structure (**a**), a single Re dopant (**b**), two Re dopants (**c**) and a Re dopant and a S vacancy (**d**). The experimental coordinates of the supercells were used as direct input to DFT to reveal the electronic band structures and the DOS (left). For comparison, the same experimental coordinates were relaxed to obtain the band structures and the DOS with DFT (middle). **e**, The areas representing the four supercells of **a–d** are highlighted in the Re-doped MoS₂ sample. Scale bar, 2 nm. **f**, Average DOS of the experimental structures in the four supercells, average DOS of the relaxed structures in the four supercells and relaxed MoS₂ DOS. **g**, PL spectra of as-synthesized pristine MoS₂ and Re-doped MoS₂ monolayers. a.u., arbitrary units.

3D atomic coordinates to DFT to reveal electronic properties of a 2D TMD in metastable states, whereas ab initio calculations relying on relaxed 3D atomic models can only predict electronic properties of the equilibrium state. With the increase of computational power in the future, the complete set of experimental 3D atomic coordinates, determined by sAET and deposited in the Materials Data Bank (www.materialsdatbank.org), can be used as direct input to DFT to correlate crystal defects with the electronic, optical, transport and chemical properties of 2D materials and heterostructures. We anticipate that sAET, coupled with DFT and the Materials Data Bank, will not only represent an important advance of ab initio calculations to better understand the structure–property relationship, but also provide feedback to materials engineering at the single-atom level.

Online content

Any methods, additional references, Nature Research reporting summaries, source data, extended data, supplementary information, acknowledgements, peer review information; details of author

contributions and competing interests; and statements of data and code availability are available at <https://doi.org/10.1038/s41563-020-0636-5>.

Received: 22 August 2019; Accepted: 11 February 2020;

Published online: 09 March 2020

References

- Butler, S. Z. et al. Progress, challenges, and opportunities in two-dimensional materials beyond graphene. *ACS Nano* **7**, 2898–2926 (2013).
- Novoselov, K. S., Mishchenko, A., Carvalho, A. & Castro Neto, A. H. 2D materials and van der Waals heterostructures. *Science* **353**, aac9439 (2016).
- Fasolino, A., Los, J. H. & Katsnelson, M. I. Intrinsic ripples in graphene. *Nat. Mater.* **6**, 858–861 (2007).
- Terrones, H., Lv, R., Terrones, M. & Dresselhaus, M. S. The role of defects and doping in 2D graphene sheets and 1D nanoribbons. *Rep. Prog. Phys.* **75**, 062501 (2012).
- Yun, W. S., Han, S. W., Hong, S. C., Kim, I. G. & Lee, J. D. Thickness and strain effects on electronic structures of transition metal dichalcogenides: 2H-MX₂ semiconductors (M = Mo, W; X = S, Se, Te). *Phys. Rev. B* **85**, 033305 (2012).

6. Warner, J. H. et al. Dislocation-driven deformations in graphene. *Science* **337**, 209–212 (2012).
7. Zhang, C. et al. Strain distributions and their influence on electronic structures of WSe_2 - MoS_2 laterally strained heterojunctions. *Nat. Nanotechnol.* **13**, 152–158 (2018).
8. Lin, Y. C., Dumcenco, D. O., Huang, Y. S. & Suenaga, K. Atomic mechanism of the semiconducting-to-metallic phase transition in single-layered MoS_2 . *Nat. Nanotechnol.* **9**, 391–396 (2014).
9. Li, H. et al. Atomic structure and dynamics of single platinum atom interactions with monolayer MoS_2 . *ACS Nano* **28**, 3392–3403 (2017).
10. Wang, S., Robertson, A. & Warner, J. H. Atomic structure of defects and dopants in 2D layered transition metal dichalcogenides. *Chem. Soc. Rev.* **47**, 6764 (2018).
11. Miao, J., Ercius, P. & Billinge, S. J. L. Atomic electron tomography: 3D structures without crystals. *Science* **353**, aaf2157–aaf2157 (2016).
12. Scott, M. C. et al. Electron tomography at 2.4-ångström resolution. *Nature* **483**, 444–447 (2012).
13. Goris, B. et al. Three-dimensional elemental mapping at the atomic scale in bimetallic nanocrystals. *Nano Lett.* **13**, 4236–4241 (2013).
14. Chen, C.-C. et al. Three-dimensional imaging of dislocations in a nanoparticle at atomic resolution. *Nature* **496**, 74–77 (2013).
15. Haberer, G. et al. Formation of bimetallic clusters in superfluid helium nanodroplets analysed by atomic resolution electron tomography. *Nat. Commun.* **6**, 8779 (2015).
16. Xu, R. et al. Three-dimensional coordinates of individual atoms in materials revealed by electron tomography. *Nat. Mater.* **14**, 1099–1103 (2015).
17. Yang, Y. et al. Deciphering chemical order/disorder and material properties at the single-atom level. *Nature* **542**, 75–79 (2017).
18. Zhou, J. et al. Observing crystal nucleation in four dimensions using atomic electron tomography. *Nature* **570**, 500–503 (2019).
19. Borisevich, A. Y., Lupini, A. R. & Pennycook, S. J. Depth sectioning with the aberration-corrected scanning transmission electron microscope. *Proc. Natl Acad. Sci. USA* **103**, 3044–3048 (2006).
20. Parr, R. G. & Yang, W. *Density-Functional Theory of Atoms and Molecules* (Oxford Univ. Press, 1989).
21. Rappe, A. M., Rabe, K. M., Kaxiras, E. & Joannopoulos, J. D. Optimized pseudopotentials. *Phys. Rev. B* **41**, 1227–1230 (1990).
22. Onida, G., Reining, L. & Rubio, A. Electronic excitations: density-functional versus many-body Green's-function approaches. *Rev. Mod. Phys.* **74**, 601–659 (2002).
23. Sigiuro, M., Huang, Y.-S., Ho, C.-H., Lin, Y.-C. & Suenaga, K. Influence of rhenium on the structural and optical properties of molybdenum disulfide. *Jpn. J. Appl. Phys.* **54**, 04DH05 (2015).
24. Zhang, K. et al. Tuning the electronic and photonic properties of monolayer MoS_2 via in situ rhenium substitutional doping. *Adv. Funct. Mater.* **28**, 1706950 (2018).
25. Yang, S. Z. et al. Rhenium-doped and stabilized MoS_2 atomic layers with basal-plane catalytic activity. *Adv. Mater.* **30**, e1803477 (2018).
26. Crowther, R. A., DeRosier, D. J. & Klug, A. The reconstruction of a three-dimensional structure from projections and its application to electron microscopy. *Proc. R. Soc. A* **317**, 319–340 (1970).
27. Frank, J. *Three-Dimensional Electron Microscopy of Macromolecular Assemblies: Visualization of Biological Molecules in Their Native State* (Oxford Univ. Press, 2006).
28. Pryor, A. et al. GENFIRE: a generalized Fourier iterative reconstruction algorithm for high-resolution 3D imaging. *Sci. Rep.* **7**, 10409 (2017).
29. Tran, K. et al. Evidence for moiré excitons in van der Waals heterostructures. *Nature* **567**, 71–75 (2019).
30. Seyler, K. L. et al. Signatures of moiré-trapped valley excitons in $\text{MoSe}_2/\text{WSe}_2$ heterobilayers. *Nature* **567**, 66–70 (2019).
31. Meyer, J. C. et al. The structure of suspended graphene sheets. *Nature* **446**, 60 (2007).
32. Meyer, J. C. et al. Direct imaging of lattice atoms and topological defects in graphene membranes. *Nano Lett.* **8**, 3582–3586 (2008).
33. Bangert, U., Gass, M. H., Bleloch, A. L., Nair, R. R. & Eccles, J. Nanotopography of graphene. *Phys. Status Solidi* **206**, 2115–2119 (2009).
34. Hofer, C. et al. Revealing the 3D structure of graphene defects. *2D Mater.* **5**, 045029 (2018).
35. Wang, W. L. et al. Direct imaging of atomic-scale ripples in few-layer graphene. *Nano Lett.* **12**, 2278–2282 (2012).
36. Miró, P., Ghorbani-Asl, M. & Heine, T. Spontaneous ripple formation in MoS_2 monolayers: electronic structure and transport effects. *Adv. Mater.* **25**, 5473–5475 (2013).
37. Brivio, J., Alexander, D. T. L. & Kis, A. Ripples and layers in ultrathin MoS_2 membranes. *Nano Lett.* **11**, 5148–5153 (2011).
38. Pavarini, E., Koch, E., Anders, F. & Jarrell, M. (eds) *Correlated Electrons: from Models to Materials* (Verlag des Forschungszentrum Jülich, 2012).
39. Wang, R. et al. Strategies on phase control in transition metal dichalcogenides. *Adv. Funct. Mater.* **28**, 1802473 (2018).
40. Voiry, D., Mohite, A. & Chhowalla, M. Phase engineering of transition metal dichalcogenides. *Chem. Soc. Rev.* **44**, 2702–2712 (2015).
41. Sun, X., Wang, Z., Li, Z. & Fu, Y. Q. Origin of structural transformation in mono- and bi-layered molybdenum disulfide. *Sci. Rep.* **6**, 26666 (2016).
42. Ciccarino, C. J., Christensen, T., Sundararaman, R. & Narang, P. Dynamics and spin-valley locking effects in monolayer transition metal dichalcogenides. *Nano Lett.* **18**, 5709–5715 (2018).
43. Komsa, H. P. & Krasheninnikov, A. V. Native defects in bulk and monolayer MoS_2 from first principles. *Phys. Rev. B* **91**, 1–17 (2015).
44. Gao, J. et al. Transition-metal substitution doping in synthetic atomically thin semiconductors. *Adv. Mater.* **28**, 9735–9743 (2016).
45. Kochat, V. et al. Re doping in 2D transition metal dichalcogenides as a new route to tailor structural phases and induced magnetism. *Adv. Mater.* **29**, 1703754 (2017).
46. Van Dyck, D., Jinschek, J. R. & Chen, F.-R. 'Big Bang' tomography as a new route to atomic-resolution electron tomography. *Nature* **486**, 243–246 (2012).
47. Chen, L.-G., Warner, J., Kirkland, A. I., Chen, F.-R. & Van Dyck, D. Snapshot 3D electron imaging of structural dynamics. *Sci. Rep.* **7**, 10839 (2017).
48. Miao, J., Ishikawa, T., Robinson, I. K. & Murnane, M. M. Beyond crystallography: diffractive imaging using coherent X-ray light sources. *Science* **348**, 530–535 (2015).
49. Jiang, Y. et al. Electron ptychography of 2D materials to deep sub-ångström resolution. *Nature* **559**, 343–349 (2018).

Publisher's note Springer Nature remains neutral with regard to jurisdictional claims in published maps and institutional affiliations.

© The Author(s), under exclusive licence to Springer Nature Limited 2020

Methods

Synthesis of Re-doped MoS₂ monolayers. Molybdenum oxide powder (99%, Sigma Aldrich), sulfur powder (99.5%, Sigma Aldrich) and ammonium perrenate (99%, Sigma Aldrich) were used as precursors for chemical vapour deposition growth⁴⁵. A selected ratio of molybdenum oxide and ammonium perrenate was added to an alumina boat with a Si/SiO₂ (285 nm) wafer cover. The furnace temperature was ramped to 550 °C in 15 min and then kept at 550 °C for another 15 min for the growth of the Re-doped MoS₂ alloy materials. We found the films to show a doping concentration of roughly 3%. Sulfur powder in another alumina boat was placed upstream, where the temperature was roughly 200 °C. After growth, the furnace was cooled to room temperature using natural convection. The growth process was carried out under 50 sccm argon at atmospheric pressure. The Re-doped MoS₂ flakes were transferred to 3-mm Quantifoil TEM grids by spin coating the samples with poly(methylmethacrylate) to support the flakes, and then were etched with KOH to release the flakes from the substrates. The sample was dipped into acetone for 2 h to wash away the poly(methylmethacrylate) and then baked in vacuum at 10⁻³ Pa and 160 °C.

Tomographic data acquisition of 2D TMDs. Two data sets, each consisting of 13 projections, were acquired from different regions of a Re-doped MoS₂ monolayer using a Nion UltraSTEM 100 aberration-corrected STEM (Supplementary Table 1). Images were collected at 60 kV in ADF-STEM mode^{50,51}. The beam convergence semi-angle was 30 mrad and the detector collection angle was in the range of 30–300 mrad, where a small detector inner angle was chosen to reduce the electron dose. The energy spread of the electron beam was 0.3 eV. A double-tilt sample holder was used to collect the data sets (Supplementary Table 2). To reduce the total electron dose, ten images per angle were measured with a beam current of 15 pA and a dwell time of 4 μs per image. To monitor any potential structural changes induced by the electron beam, the first and last projections of each data set were compared to ensure that no noticeable structural changes were observed during data acquisition (Supplementary Fig. 2).

Drift correction. To reduce the sample drift effect on data acquisition, we took ten STEM images for each tilt angle and aligned them using the following procedure. First, we chose a region of 300 × 300 pixels from the first image as a reference. Next, a region of 200 × 200 pixels from the next image was cropped and scanned over the reference image with a step size of 0.1 pixel to calculate the cross-correlation coefficients. The maximum cross-correlation coefficient corresponds to the relative drift between the two images. Typically, the drift between two neighbouring images is less than 1 pixel. By repeating this process, the relative drift for all ten images was determined and an overall drift vector was calculated. With the drift vector, we applied scan distortion correction by assuming that the drift vector is uniformly distributed along the slow-scan direction during STEM image acquisition. Thus, the drift for each pixel in the image was determined and a drift-corrected image was formed by interpolating the non-corrected image onto the drift-corrected pixel positions. After applying drift correction, we averaged the ten images to obtain a final image for each tilt angle.

Image denoising. The raw ADF-STEM images contain mixed Poisson and Gaussian noise, and a block-matching and 3D filtering (BM3D) algorithm was applied to denoise the average image of each tilt angle⁵². Two different sets of denoising parameters were applied for the BM3D: one is the exact noise level estimated from the experimental images (termed BM3D 100%), and the other is obtained by doubling the estimated noise level (termed BM3D 200%). There are two reasons for the use of BM3D 100% and 200%. First, this allows us to cross-validate the reconstructions with different denoising parameters. Second, the BM3D 100% reconstruction provides better contrast between the Re, Mo and S atoms, while BM3D 200% produces better reconstruction for the S atoms. All these post-processing and denoising methods have been previously demonstrated to be robust for dealing with ADF-STEM images^{14,16–18}.

Angle calibration and 3D coordinate fitting of the Re and Mo atoms. The nominal angles were measured using a Nion double-tilt stage (Supplementary Table 2). After denoising each projection, we determined the *x* and *y* coordinates of each Re and Mo atom by fitting a 2D Gaussian in a 5 × 5 pixel region. According to a geometric relation, the *x* and *y* coordinates of the Re and Mo atoms in each data set change as a function of the tilt angle. To calibrate the tilt angles and determine the 3D coordinates of the Re and Mo atoms, we used the least-square method to minimize the following equation:

$$E = \sum_i \sum_j \left\{ \left[P_x(\mathbf{r}_i, \alpha_j, \beta_j) - x_i^j \right]^2 + \left[P_y(\mathbf{r}_i, \alpha_j, \beta_j) - y_i^j \right]^2 \right\} \quad (1)$$

where P_x and P_y are the functions of projecting the 3D coordinates of the Re and Mo atoms to the *x* and *y* coordinates in the projections, respectively, \mathbf{r}_i is the 3D coordinates of the *i*th Re or Mo atom, α_j and β_j are the tilt angles of the *j*th projection and x_i^j and y_i^j are the measured *x* and *y* coordinates of the *i*th atom in the *j*th projection, respectively. By minimizing E , we calibrated the tilt angles of the 13 projections (Supplementary Table 2) and obtained the 3D coordinates of all the Re

and Mo atoms in each data set (Extended Data Fig. 3). This least-square fitting method is robust and produces consistent results regardless of different initial inputs.

Deconvolution for vibrational correction. Due to the high length/thickness ratio and the free-standing structure, we observed that the 2D TMD suffered from vibrational blurring along the direction perpendicular to the TEM grid during data acquisition. The vibrational blurring is equivalent to convolving the images with a kernel and can be removed through deconvolution if the blurring kernel is known. In this experiment, the blurring kernel was estimated on the basis of the fact that all atoms should be spherical. We performed deconvolution using the following procedure. First, we interpolated each experimental image by a factor of 2 with linear interpolation and cropped a region of 100 × 100 pixels without Re dopants. Second, a MoS₂ model of the same experimental tilt angle was used to create a reference image of the same size as the cropped experimental image but with spherical atoms. The reference image was normalized and aligned with the experimental image. Third, a vibrational kernel was constructed by adjusting the vibrational direction, vibration amplitude and Gaussian blurring. The experimental image was deconvolved with the constructed kernel using the Lucy–Richardson algorithm^{53,54} and compared with the reference image. A brute-force process was conducted until an optimal kernel was obtained, creating the best match between the experimental and reference images. Finally, the optimal kernel was applied to the whole experimental image using the Lucy–Richardson algorithm. The deconvolved image was binned to be its original scale. A comparison between before and after deconvolution is shown in Supplementary Fig. 3.

Image partition and reconstruction with sAET. To implement sAET, we chose a 3D window of 60 × 60 × 60 voxels and scanned it along the *x* and *y* axes with a step size of 30 voxels. This step size offsets each partition to include a 30-voxel overlap between neighbouring partitions on each side. At each step, the corresponding regions from all 13 projections in each data set were cropped and grouped into an image stack. Each image stack consists of 13 images with varied shapes, corresponding to the projection of the 3D window along different tilt angles. After a full 2D scan was completed, all the projections were partitioned into image stacks. All the image stacks were aligned and reconstructed in parallel by the GENFIRE algorithm²⁸. Each GENFIRE reconstruction used a 33-voxel support along the *z* axis and ran 1,000 iterations. Due to the extended nature of the 2D TMD along the *x* and *y* axes, the reconstruction of each image stack contained artefacts near the boundary. To remove these artefacts, we stitched together only the central 30 × 30 × 33 voxels of the reconstructed windows to produce a full 3D reconstruction. By applying this partition and reconstruction procedure, we obtained the full 3D reconstructions of both the BM3D 100% and 200% projections of each data set.

Initial localization of 3D atomic coordinates and species. The 3D atomic coordinates and species of the 2D TMD were initially traced from the 3D reconstructions using the following procedure. We first identified all local maxima in the BM3D 200% reconstruction of each data set. Starting from the highest-intensity local maximum peak, we cropped a 1.71 × 1.71 × 1.71 Å³ (5 × 5 × 5 voxel) volume with the selected local peak as the centre. We fitted the volume with a 3D Gaussian function described elsewhere^{16–18}. If a fitted peak position was a minimum distance of 1.6 Å away from any previously fitted peak (that is, a minimum-distance constraint), we added it to a list of potential atoms. By applying the 3D Gaussian fitting algorithm to all the identified atoms, we obtained a complete list of potential atom positions. These positions were manually checked to correct for unidentified or misidentified atoms due to fitting failure or areas with connected intensity blobs from multiple atoms. We then assigned the atomic species on the basis of the 3D intensity distribution of the traced potential Re, Mo and S atoms.

Refinement of 3D atomic coordinates and species and identification of S vacancies. The traced 3D atomic coordinates and species were refined by the following procedure. First, each experimental image of BM3D 100% was converted to Fourier slices $F_{\text{obs}}^j(\mathbf{q})$ with $j = 1, \dots, 13$ using the fast Fourier transform. Next, 13 Fourier slices were calculated with the atomic model using

$$F_{\text{calc}}^j(\mathbf{q}) = \sum_{n=1}^{N_a} H f_c(\mathbf{q}) e^{-\frac{B^j q^2}{4} - 2\pi i \mathbf{r}_n \cdot \mathbf{q}} \quad (2)$$

where N_a is the number of atoms, H is the scaling factor for different atomic species, the B^j factor accounts for the electron-probe size, the missing wedge and the thermal motion of each atomic species, $f_c(\mathbf{q})$ is a normalized electron scattering factor and \mathbf{r}_n is the 3D position of the *n*th atom. An error function was then calculated using

$$E = \sum_{j=1}^{13} \sum_{\mathbf{q}} \left| F_{\text{obs}}^j(\mathbf{q}) - F_{\text{calc}}^j(\mathbf{q}) \right|^2 \quad (3)$$

which was minimized with respect to the \mathbf{r}_n by a gradient descent method^{16–18}.

From the refined 3D atomic model, we developed an atom pair flipping method to identify the S vacancies, which consists of the following four steps. First, we randomly chose a pair of S atoms between the top and bottom atomic layers. For each selected S pair, projection images were calculated for all the tilt angles by flipping the pair among four cases: (1) both atoms are S, (2) both are vacancies, (3) the top is a S atom and the bottom is a vacancy and (4) the top is a vacancy and the bottom is a S atom. Four atomic models were generated according to the four cases, with the same H and B' factors. Second, four sets of 13 projections with the experimental tilt angles were calculated from the atomic models. An R_1 factor was computed between measured and calculated projections,

$$R_1^j = \frac{\sum_{x,y} |f_{\text{obs}}^j(x,y) - f_{\text{calc}}^j(x,y)|}{\sum_{x,y} |f_{\text{obs}}^j(x,y)|} \quad (4)$$

$$R_1 = \frac{\sum_j R_1^j}{13} \quad (5)$$

where $f_{\text{calc}}^j(x,y)$ and $f_{\text{obs}}^j(x,y)$ are the j th measured and calculated projections. As flipping a pair of atoms only affects a small cylindrical volume for each tilt angle, we only calculated a small area of projection along a cylindrical volume containing the atom pair. By comparing the R_1 factor among the four cases, the one with the smallest error R_1 was chosen and updated in the atomic model. Third, we repeated the first two steps for all the S atom pairs and obtained an updated 3D atomic model. A global scale factor was calculated for the updated atomic model to minimize the error between the measured and calculated projections. Fourth, we iterated steps one to three for all the S atom pairs until there was no change in the atomic species. The atom pair flipping method was robust and converged after a few iterations for both data sets. After identifying all the S vacancies, we refined the 3D atomic coordinates once more using equations (2) and (3).

Dynamic refinement of the S atoms near the Re atoms. Due to the use of a low-energy electron beam (60 keV) and a small detector inner angle to reduce the electron dose, we observed the dynamic scattering effect of the Re atoms (see the next section for details), which influenced some nearby S atoms. We implemented a brute-force approach to perform dynamic refinement of these Re and S atoms. We first identified those S atoms near the Re atoms that either violated a minimum distance of 1.6 Å (caused by the refinement) or deviated from the S atomic layer more than 1 Å. There were 11 and 13 such S atoms in data sets 1 and 2, respectively. For each of these S and Re atoms, we performed a 3D scan of its position with a range of ± 40 pm along the x and y axes and ± 120 pm along the z axis. The step sizes are 20 pm, 20 pm and 30 pm along the x , y and z axes, respectively. At each scanning step, we used multislice simulations to calculate 13 projection images 40×40 pixels in size at different tilt angles and computed the R_1 factor relative to the measured images. The S atom in the atomic model was updated to the position corresponding to the minimum R_1 factor. We repeated this dynamic refinement procedure for all the S atoms whose positions were influenced by nearby Re atoms.

Multislice simulations for precision estimation. We performed multislice simulations to estimate the 3D precision of the atomic coordinates and species^{55,56}. The experimental atomic model was placed in a rectangular supercell. The supercell was divided into multiple 2-Å slices along the z axis, and the x - y plane was discretized into $1,920 \times 1,920$ pixels. The same experimental parameters were used for the multislice simulations (energy, 60 keV; the third order spherical aberration C_3 , 0 mm; the fifth order spherical aberration C_5 , 5 mm; convergence semi-angle, 30 mrad; detector inner angle, 30 mrad; detector outer angle, 300 mrad). Each STEM image was generated by a raster scan in the x - y plane with a step size of 0.34 Å. For each tilt angle, we averaged 12 phonon configurations to obtain a projection image. The image was convolved with a 5×5 -pixel Gaussian kernel ($\sigma = 1.0$) to account for the electron-probe size, thermal vibrations and other incoherent effects. The mixture of Gaussian and Poisson noise determined from the experimental images was added to the multislice images (Extended Data Fig. 4). From the 13 multislice images of data set 1, we used the same imaging processing, sAET reconstruction, atom tracing and refinement procedures to obtain a new 3D atomic model. By comparing it with the experimental 3D atomic model, we found that all the atom species were correctly identified, including all S vacancies. The RMSDs of the S, Re and Mo atoms were 15 pm, 12 pm and 4 pm, respectively (Fig. 1b).

Next, we performed multislice simulations using the same parameters except for changing the detector inner angle to 50 mrad. We added Gaussian and Poisson noise to the multislice projections with the same electron dose and obtained another 3D atomic model. In comparison with the experimental atomic model, all the atom species were correctly identified and the RMSDs of the S, Re and Mo atoms were 18 pm, 3 pm and 3 pm, respectively. Compared with the 30-mrad detector inner angle results, the RMSD of the Re atoms is decreased due to the reduced dynamic scattering effect, while the RMSD of the S atoms is increased due to the weaker intensity in the 50-mrad detector inner angle case.

Measurement of the 3D strain tensor of Re-doped MoS₂. The strain tensor was determined from the experimental 3D atomic coordinates using a procedure described elsewhere¹⁶. The experimental atomic model of each data set was least-square fitted to an ideal MoS₂ model. The displacement vectors, $\Delta\mathbf{u}$, were calculated as the difference in the atomic positions between the experimental and ideal models. Each displacement component (Δx , Δy , Δz) was interpolated to a cubic grid through kernel density estimation⁵⁷. A 3D Gaussian kernel with $\sigma = 3.16$ Å was convolved with the displacement fields, which increases the precision of the strain tensor measurement, but reduces the resolution. The six components of the strain tensor of the two data sets are shown in Extended Data Fig. 6.

To determine the principal strain of the four supercells in Fig. 5, we calculated the average strain tensor within each supercell and then solved for the eigenvalues and eigenvectors of the average strain tensor. The principal strain and three corresponding directions are [0.4%, -0.23%, -1.15%], [0.86, 0.20, 0.47], [0.15, 0.79, -0.60] and [-0.49, 0.58, 0.65] for supercell A, [0.5% -1.00%, -0.60%], [-0.87, -0.37, -0.32], [-0.48, 0.75, 0.44] and [0.08, 0.54, -0.84] for supercell B, [0.14%, -0.71%, -1.58%], [0.93, 0.37, 0.04], [-0.37, 0.92, 0.10] and [0.00, -0.11, 0.99] for supercell C and [-0.04%, -1.84%, 1.35%], [-0.92, -0.20, 0.34], [-0.26, 0.95, -0.15] and [0.30, 0.23, 0.92] for supercell D.

Data availability

The raw and processed experimental data and all the MATLAB source codes for the image reconstruction and data analysis will be freely available at www.physics.ucla.edu/research/imaging/sAET immediately after this work is published. The experimental 3D atomic coordinates of the two data sets will be deposited in the Materials Data Bank (MDB, www.materialsdatbank.org), with their MDB IDs provided in Supplementary Table 1.

References

- Muller, D. A. Structure and bonding at the atomic scale by scanning transmission electron microscopy. *Nat. Mater.* **8**, 263–270 (2009).
- Pennycook, S. J. & Nellist, P. D. *Scanning Transmission Electron Microscopy* (Springer, 2011).
- Dabov, K. & Foi, A. & Katkovnik, V. & Egiazarian, K. Image denoising with block-matching and 3D filtering. *Proc. SPIE* **6064**, 606414 (2006).
- Richardson, W. H. Bayesian-based iterative method of image restoration. *J. Opt. Soc. Am.* **62**, 55 (1972).
- Lucy, L. B. An iterative technique for the rectification of observed distributions. *Astron. J.* **79**, 745 (1974).
- Kirkland, E. J. *Advanced Computing in Electron Microscopy* (Springer, 2010).
- Pryor, A., Ophus, C. & Miao, J. A streaming multi-GPU implementation of image simulation algorithms for scanning transmission electron microscopy. *Adv. Struct. Chem. Imaging* **3**, 15 (2017).
- Parzen, E. On estimation of a probability density function and mode. *Ann. Math. Stat.* **33**, 1065–1076 (1962).

Acknowledgements

We thank M. F. Chisholm for support of the STEM experiment and C. Ophus for help with data analysis. This work was primarily supported by the US Department of Energy (DOE), Office of Science, Basic Energy Sciences (BES), Division of Materials Sciences and Engineering under award DE-SC0010378. It was also supported by STROBE: a National Science Foundation (NSF) Science and Technology Center under award DMR-1548924, by an Army Research Office MURI grant on Ab-Initio Solid-State Quantum Materials: Design, Production and Characterization at the Atomic Scale, and by the Division of Materials Research of the US NSF under award DMR-1437263. P.M.A. acknowledges support from the Air Force Office of Scientific Research under award FA9550-18-1-0072. The STEM experiment was conducted at the Center for Nanophase Materials Sciences, which is a DOE Office of Science User Facility.

Author contributions

J.M. conceived and directed the project. Y.G. and P.M.A. synthesized the Re-doped MoS₂ sample and measured the PL and Raman spectra, S.Y., X.T., D.S.K., J.C.I. and J.M. planned and/or performed the STEM experiments and X.T., D.S.K., J.M., Yongsoo Yang, Yao Yang and Y. Yuan discussed and/or performed 3D reconstruction, atom tracing and data analysis. C.J.C., B.D., P.N., D.S.K., X.T. and J.M. discussed and/or carried out DFT calculations. J.M., X.T. and D.S.K. wrote the manuscript with help and/or comments from all authors.

Competing interests

The authors declare no competing interests.

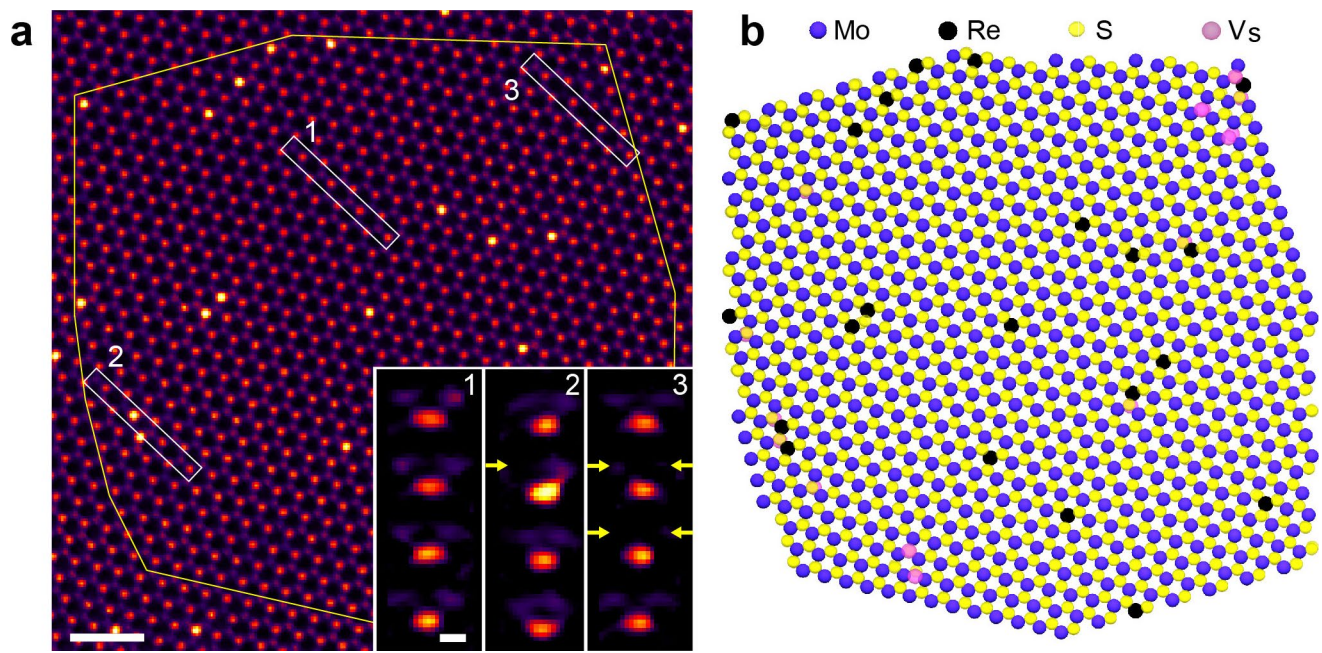
Additional information

Extended data is available for this paper at <https://doi.org/10.1038/s41563-020-0636-5>.

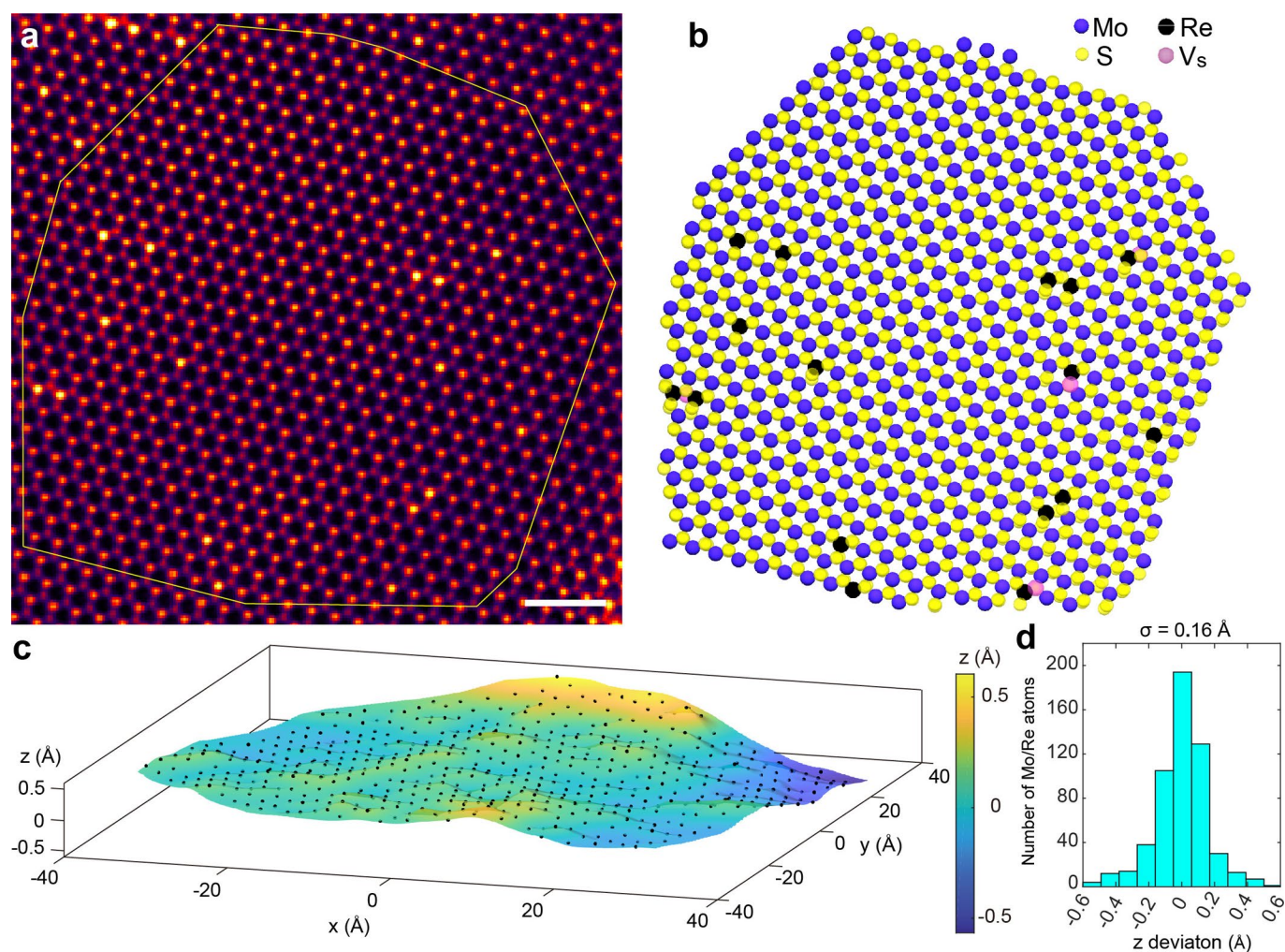
Supplementary information is available for this paper at <https://doi.org/10.1038/s41563-020-0636-5>.

Correspondence and requests for materials should be addressed to J.M.

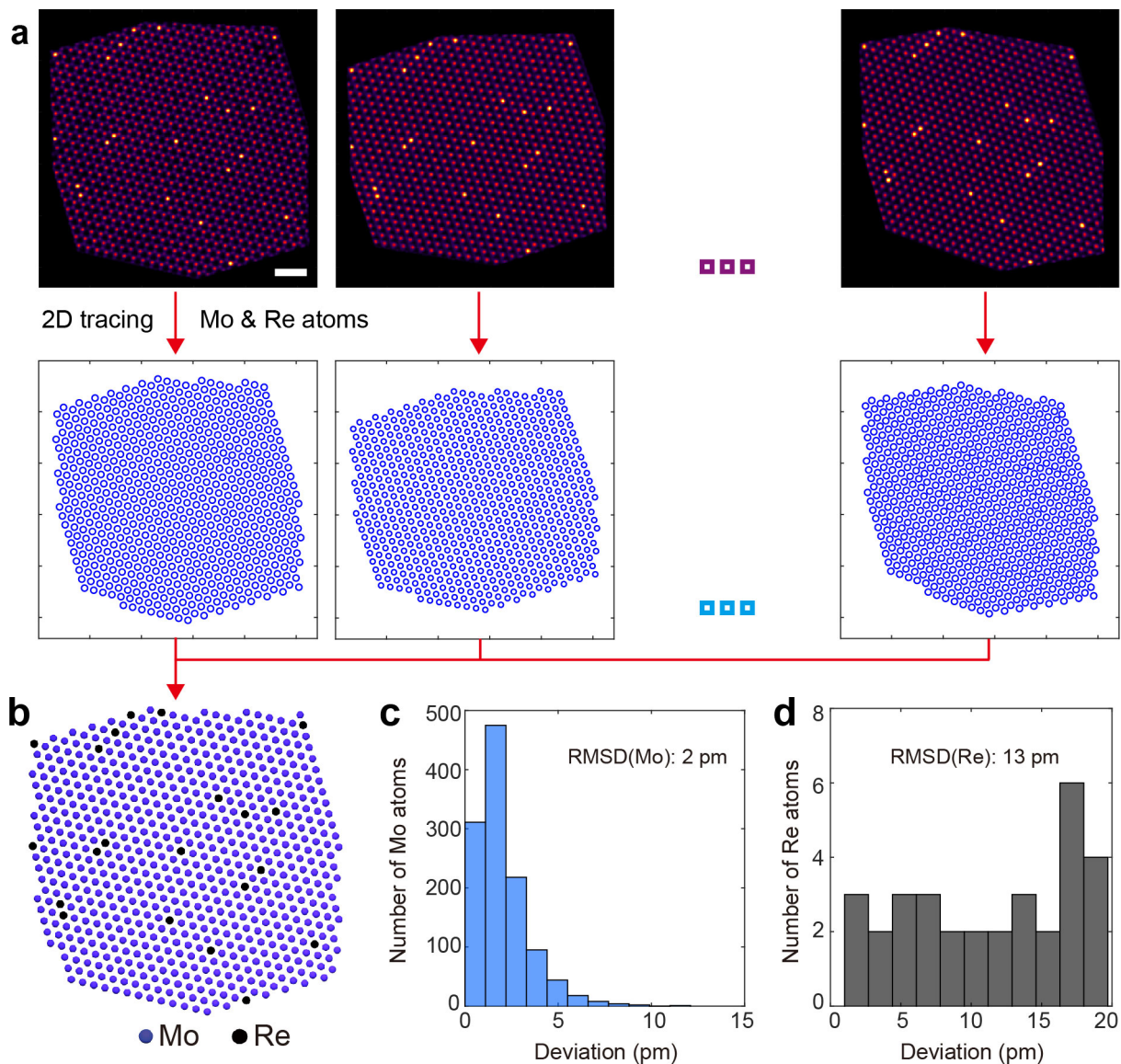
Reprints and permissions information is available at www.nature.com/reprints.



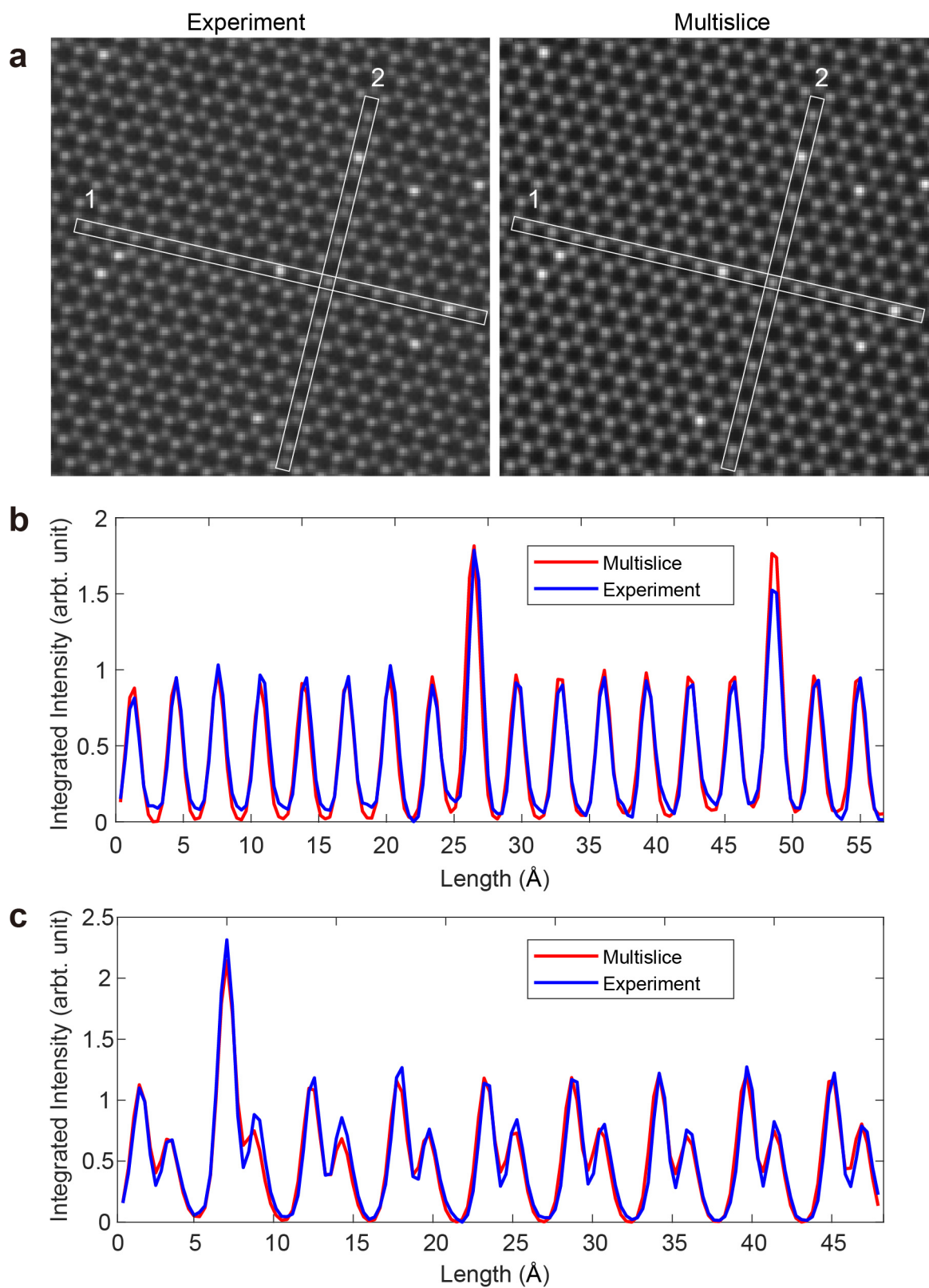
Extended Data Fig. 1 | 3D atomic coordinates and crystal defects in data set 1. **a**, Top view of the 3D reconstruction of data set 1. The inset shows the side view of MoS_2 (panel 1), MoS_2 with a Re dopant and a S vacancy (panel 2), and MoS_2 with 3 S vacancies (panel 3), where arrows indicate the vacancies. Scale bar, 1 nm and scale bar (inset), 2 Å. **b**, 3D atomic model of the bounded region in (a), consisting of 1381 S, 686 Mo and 21 Re atoms with 15 S vacancies.



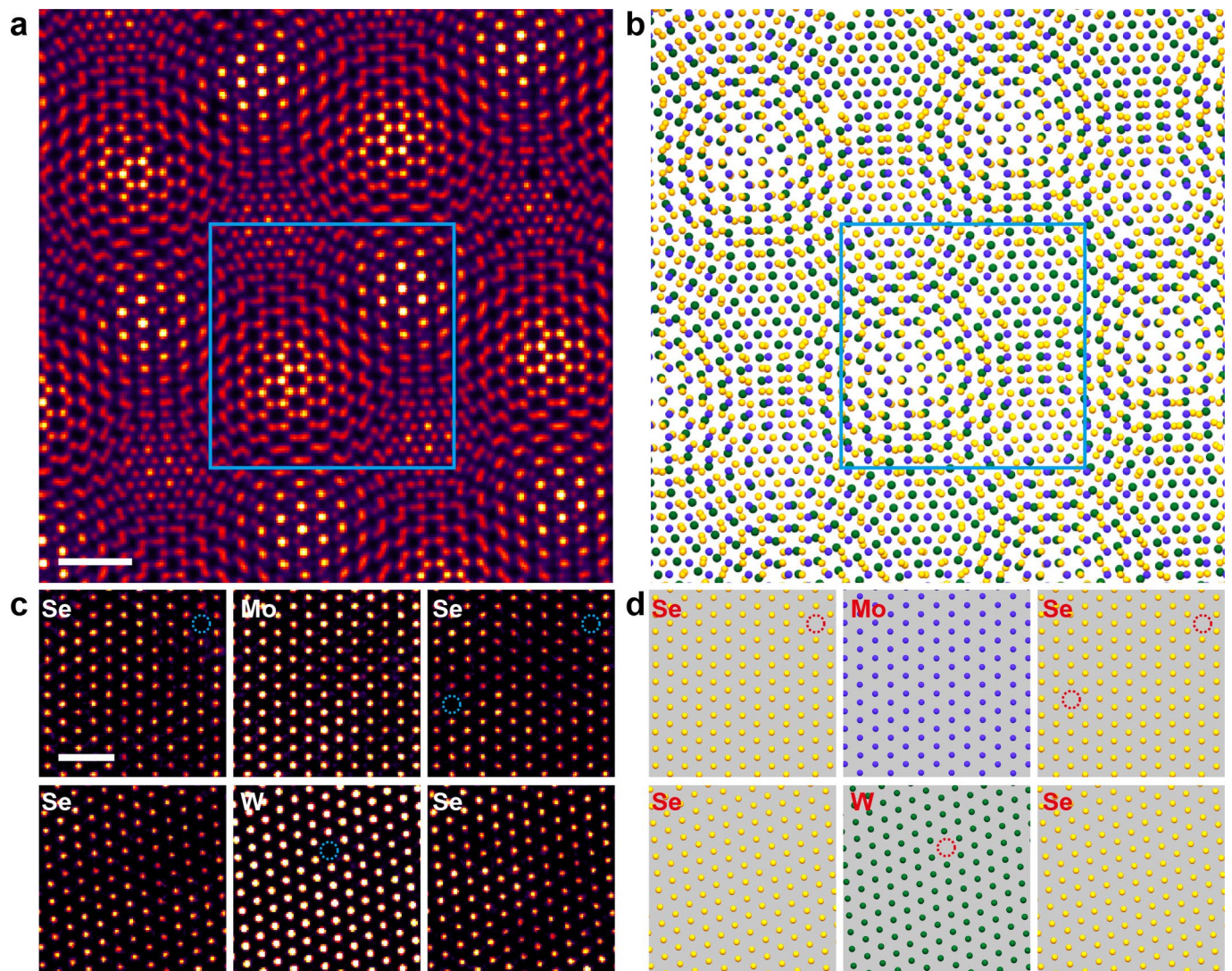
Extended Data Fig. 2 | 3D atomic coordinates and crystal defects in data set 2. **a**, Top view of the 3D reconstruction. Scale bar, 1 nm. **b**, 3D atomic model of the bounded region in **(a)**, consisting of 1083 S, 531 Mo and 16 Re atoms with 4 S vacancies. **c**, 3D plot of the Mo/Re layer showing atomic-scale ripples, where the dots represent the Mo/Re atoms. **d**, Histogram of the distribution of the z coordinates of the Mo/Re atoms in data set 1 with a standard deviation (σ) of 0.16 Å.



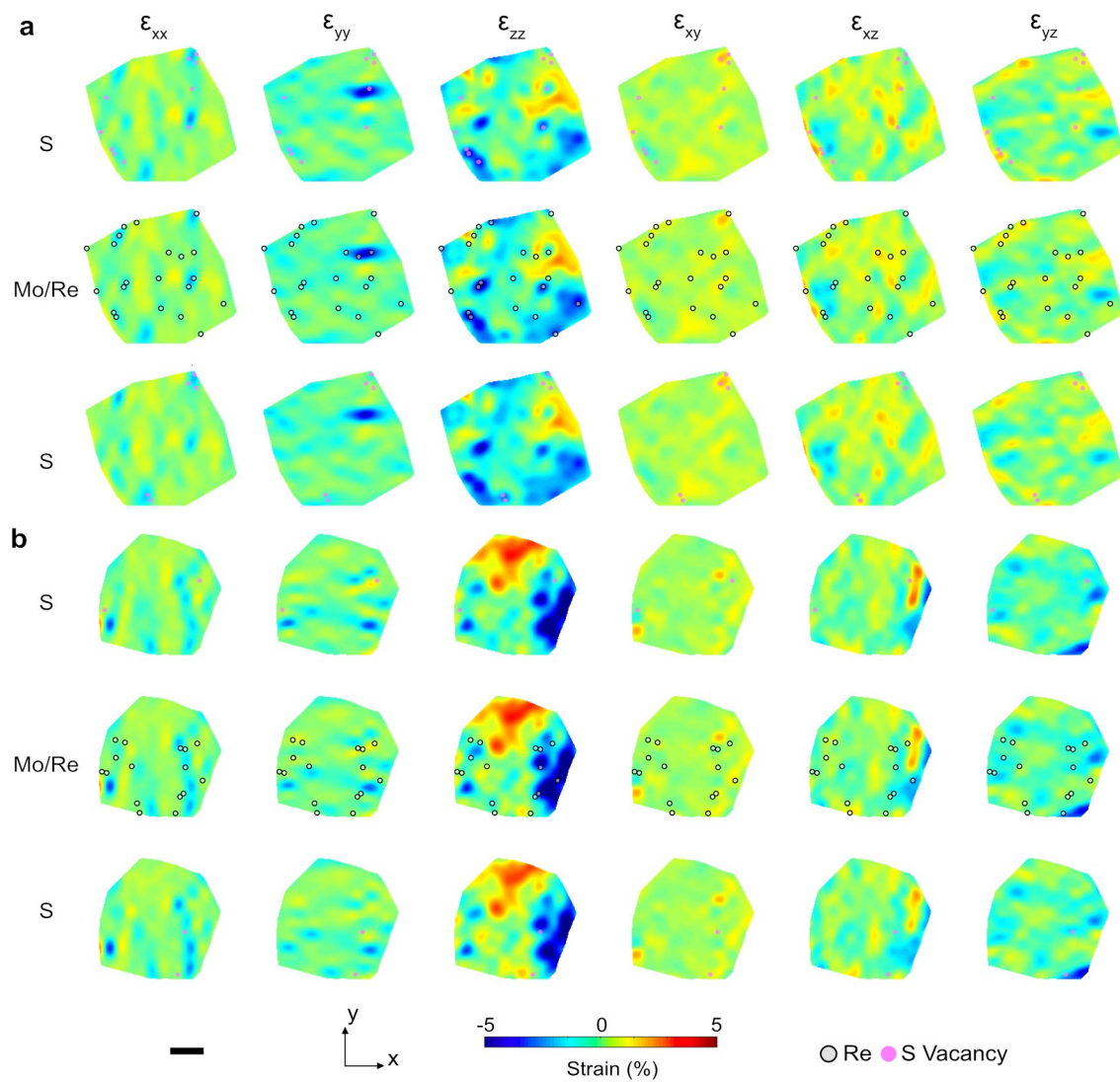
Extended Data Fig. 3 | Least square fitting to determine the 3D coordinates of the Re and Mo atoms. a, The x and y coordinates of the Re and Mo atoms were localized from the aligned projections of each data set. **b**, From these 2D coordinates, the tilt angles were calibrated and the 3D coordinates of the Re and Mo atoms were determined for each data set. The 3D atomic coordinates are consistent with those obtained by sAET with a RMSD of 2 pm and 13 pm for Mo (**c**) and Re (**d**) atoms, respectively, where a total of 1176 Mo and 32 Re atoms was used in the statistical analysis. Scale bar, 1 nm.



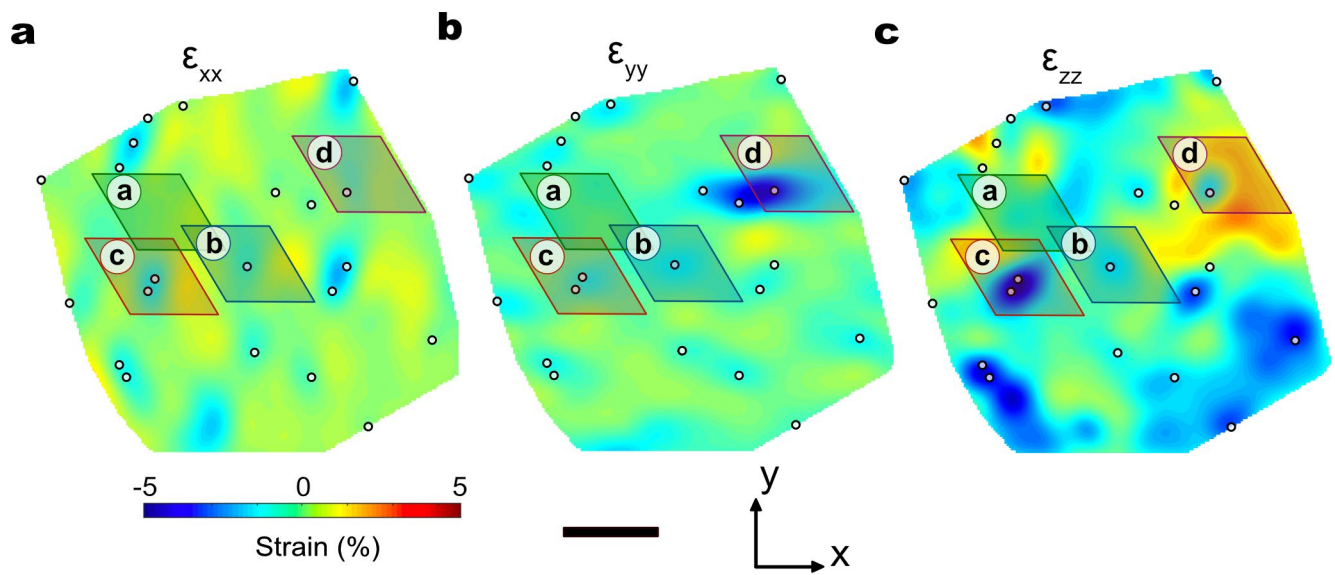
Extended Data Fig. 4 | Multislice simulation results. **a**, The experiment image versus the multislice image of the same region. **b** and **c**, The intensity profiles corresponding to labelled regions 1 and 2 in **(a)**, where the high, medium and low intensity peaks represent the Re, Mo and S atoms, respectively.



Extended Data Fig. 5 | Numerical simulations on the sAET reconstruction of a $\text{MoSe}_2\text{-WSe}_2$ heterostructure with moiré patterns. **a**, Top view of the 3D reconstruction of double-layered heterostructure from 15 multislice projections with a double tilt range from -25° to $+25^\circ$. **b**, Top view of 3D atomic model obtained from **(a)**, where a 5° rotational mismatch between the top and bottom layers is visible. **c**, 6 atomic layers of the 3D reconstruction in the square region in **(a)**, where atomic defects in each layer are labelled as blue circles. **d**, 6 atomic layers of the 3D model in the square region in **(b)**, where traced defects are shown as red circles. The RMSD between the sAET reconstruction and the original atomic model is 8 pm, 5 pm and 13 pm for Mo, W and Se atoms, respectively.



Extended Data Fig. 6 | Full 3D strain tensor of data set 1 (a) and data set 2 (b). The six strain components are shown from left to right columns, and the three atomic layers are displayed from top to bottom. Scale bar, 2 nm.



Extended Data Fig. 7 | Strain tensor maps of ϵ_{xx} (a), ϵ_{yy} (b), ϵ_{zz} (c) of the Mo/Re layer in the four supercells used in DFT calculations. The four $6 \times 6 \times 1$ supercells labelled with (a), (b), (c) and (d) correspond to those in Fig. 5e. Scale bar, 2nm.